Quantitative biophysical metrics for rapid evaluation of ovarian cancer metastatic potential

Apratim Mukherjee[a], Haonan Zhang[a], Katherine Ladner[b], Megan Brown[c], Jacob Urbanski[a], Joseph P. Grieco[c], Rakesh K. Kapania[d], Emil Lou[b], Bahareh Behkam[a,*], Eva M. Schmelz[c,*], and Amrinder S. Nain[a,*]

[a]Department of Mechanical Engineering and [d]Department of Aerospace and Ocean Engineering, Virginia Tech, Blacksburg, VA 24060; [b]Division of Hematology, Oncology and Transplantation, Masonic Cancer Center, University of Minnesota, Minneapolis, MN 55455; [c]Department of Human Nutrition, Foods and Exercise, Virginia Tech, Blacksburg, VA 24060

ABSTRACT **Ovarian cancer is routinely diagnosed long after the disease has metastasized through the fibrous submesothelium. Despite extensive research in the field linking ovarian cancer progression to increasingly poor prognosis, there are currently no validated cellular markers or hallmarks of ovarian cancer that can predict metastatic potential. To discern disease progression across a syngeneic mouse ovarian cancer progression model, here we fabricated extracellular matrix mimicking suspended fiber networks: cross-hatches of mismatch diameters for studying protrusion dynamics, aligned same diameter networks of varying interfiber spacing for studying migration, and aligned nanonets for measuring cell forces. We found that migration correlated with disease while a force-disease biphasic relationship exhibited F-actin stress fiber network dependence. However, unique to suspended fibers, *coiling* occurring at the tips of protrusions and not the length or breadth of protrusions displayed the strongest correlation with metastatic potential. To confirm that our findings were more broadly applicable beyond the mouse model, we repeated our studies in human ovarian cancer cell lines and found that the biophysical trends were consistent with our mouse model results. Altogether, we report complementary high throughput and high content biophysical metrics capable of identifying ovarian cancer metastatic potential on a timescale of hours.**

Monitoring Editor
Dennis Discher
University of Pennsylvania

Received: Aug 26, 2021
Revised: Dec 16, 2021
Accepted: Dec 22, 2021

This article was published online ahead of print in MBoC in Press (http://www.molbiolcell.org/cgi/doi/10.1091/mbc.E21-08-0419) on January 5, 2022.

Data availability statement: The data that support the findings of this study are available from the corresponding author on reasonable request.

Author contributions: A.S.N. and B.B. conceived the research. A.S.N., E.M.S., B.B., and E.L. designed and supervised the research. A.M., H.Z., M.B., K.L., and J.G. performed the experiments. R.K.K. and A.S.N. developed the analytical and finite element models to calculate cell forces. A.M., M.B., H.Z., K.L., J.G., and J.U. conducted the analysis. A.M. wrote the manuscript. A.M., B.B., E.M.S., E.L., R.K.K., and A.S.N. edited the manuscript.

Competing interests: The authors declare no competing interests.

*Address correspondence to: Bahareh Behkam (behkam@vt.edu); Eva M. Schmelz (eschmelz@vt.edu); Amrinder Nain (nain@vt.edu).

Abbreviations used: ECM, extracellular matrix; FAC, focal adhesion cluster; MLCK, myosin light chain kinase; MOSE, mouse ovarian surface epithelial model; NFM, nanonet force microscopy; PBS, phosphate-buffered saline; pMLC, phosphorylated myosin light chain; STEP, spinneret-based tunable engineered parameters.

INTRODUCTION

Ovarian cancer is the fifth leading cause of cancer-related deaths in women. It presents the highest mortality rate of any other gynecological cancer, with ~54% of patients dying from the initial or recurrent diagnosis (Ozga *et al.*, 2013; Novak *et al.*, 2018). Due to the lack of early detection capabilities, only ~30% of patients are diagnosed when the cancer is limited to the ovaries (Stage I), presenting the highest chance of cure (Dinkelspiel *et al.*, 2015; Torre *et al.*, 2018). The chances of survival decline dramatically with ovarian cancer progression, including metastasis to the pelvic organs (Stage II), the peritoneal organs (Stage III), or beyond the peritoneal cavity (Stage IV) (Cannistra, 2004; Bast *et al.*, 2009). Despite recent developments in early-stage screening and diagnostic technologies for other types of cancer, the diagnostic tools for ovarian cancer remain primarily limited to biannual pelvic examinations, transvaginal ultrasounds, or cancer antigen (CA) 125 blood tests (Goff *et al.*, 2000; Rustin, 2002; Jelovac and Armstrong, 2011; Doubeni *et al.*, 2016; Rojas *et al.*, 2016). Furthermore, the diagnostic tools of ovarian cancer may not

be able to detect early stages of the disease, distinguish between disease stages and metastatic potential, or are not routinely performed. Genetic profiling of biopsies, circulating tumor cells, or bodily fluids are used to screen for specific mutations or secreted proteins; however, the genetic or protein markers are often only applicable to a subset of patients due to the inherent heterogeneity of tumors (Phillips-Chavez *et al.*, 2020) or do not include epigenetic changes, miRNA, circular RNA, exosomes, or stimuli from other cells in the tumor microenvironment that all can contribute to disease progression (Tran *et al.*, 2020). Thus there exists a currently unmet critical need for the development of diagnostic tools that can determine the disease stage in a timely and reliable manner and consequently improve the likelihood of patient recovery.

The metastatic cascade in ovarian cancer progression begins with the exfoliation of the cancer cells from the primary site, such as the ovary or the fallopian tubes (Kenny *et al.*, 2014). Subsequently, the cancer cells are circulated in the peritoneal cavity by the peritoneal serous fluid or ascites flow and adhere to secondary sites such as the omentum and other peritoneal organs, including the liver, diaphragm, and intestines that are lined with a protective layer of mesothelial cells (Lengyel, 2010; Novak *et al.*, 2018; El Aziz *et al.*, 2019). The adherent ovarian cancer cells then begin invading through the mesothelial cell monolayers into the submesothelial connective tissue stroma, which is a fibrous network predominantly composed of collagen fibers (Wilkosz *et al.*, 2005). Invasion of the ovarian cancer cells through the mesothelial monolayer occurs by either pushing the mesothelial cells aside by exerting physical forces (Niedbala *et al.*, 1985; Iwanicki *et al.*, 2011), by cleaving the mesothelial monolayer via matrix metalloproteinases (Huang, 2002; Satpathy *et al.*, 2009), or by apoptosis (Heath *et al.*, 2004), thus creating a pathway to the underlying fibrous extracellular matrix (ECM).

Cell invasion is a highly orchestrated sequence of events that is initiated with the extension of protrusions from the main cell body first to sense the surrounding fibrous environment and establish polarity (Friedl and Wolf, 2003). Subsequently, cells can form integrin-mediated stable focal adhesions necessary to generate actomyosin contractility-based forces (Munevar *et al.*, 2001; Kraning-Rush *et al.*, 2012) and invade through the submesothelial ECM (Beningo *et al.*, 2001; Plotnikov *et al.*, 2012; Reig *et al.*, 2014). Not surprisingly, a combination of in vitro and in vivo studies have thus explored the potential of characterizing protrusion dynamics, migration, and force transmission by cancer cells as alternative biophysical indicators of their metastatic potential complementary to genetic modifications (Condeelis and Segall, 2003; Zijlstra *et al.*, 2008; Indra *et al.*, 2011; Carey *et al.*, 2012; Gligorijevic *et al.*, 2012; Leong *et al.*, 2014; Stoletov *et al.*, 2018). Biophysical metrics have been used to characterize a variety of cells including breast cancer (Carlsen *et al.*, 2015), liver cancer (Pepin *et al.*, 2015), brain cancer (Pepin *et al.*, 2015), chondrosarcoma (Darling *et al.*, 2007), and fibroblasts (Phillip *et al.*, 2017) using a range of technologies that include magnetic resonance elastography, ultrasound elastography, cell-based sensors, atomic force microscopy, optical tweezers, and microfluidic platforms (Yadav *et al.*, 2019; Yankaskas *et al.*, 2019). However, most of the in vitro measurements are performed on flat, 2D surfaces that only partially recapitulate the complex, fibrous architecture of the submesothelial ECM. Three-dimensional gels are more analogous to the in vivo environments, but their inherent spatial heterogeneity can hinder the quantitation of biophysical metrics as metastatic indicators in a repeatable manner.

The highly aggressive serous ovarian cancer is now thought to originate in the fallopian tubes (Eckert *et al.*, 2016). Differences in gene expression between ovarian and fallopian tube cancer, in addition to interindividual differences in gene expression, the heterogeneity of ovarian cancer histology, and its tissue of origin, add to the difficult task of identifying early stages of ovarian cancer (Merritt *et al.*, 2013). Thus while recent studies have characterized changes in genetic expression between 25 different ovarian cancer cell lines (Ince *et al.*, 2015) and cell–stroma interaction across a range of ovarian cancer cell lines of varying metastatic characteristics from benign to highly metastatic, these cell lines still typically originate from different patient samples (Alkmin *et al.*, 2020).

In this study, we used the nonelectrospinning, spinneret-based tunable engineered parameters (STEP; Sharma *et al.*, 2013; Nain and Wang, 2013; Wang and Nain, 2014) platform to construct controlled and suspended nanofiber networks that mimic fibrous features of the submesothelial ECM (Dobbie *et al.*, 1981; Thomas, 1987). We utilized multiple fibrous architectures to inquire if protrusions, migration, and forces can be used as markers of metastatic potential in our previously reported syngeneic mouse ovarian surface epithelial (MOSE) cell model (Roberts *et al.*, 2005; Cohen *et al.*, 2013, 2016) which allows us to eliminate both the interindividual and the histological differences that are inherently associated with using cells from different patient samples or origin sites, respectively. The MOSE model is representative of the disease progression from early to late stages of human serous ovarian cancer and comprises of the benign MOSE-E, the tumorigenic, slow-developing disease MOSE-L (lethal disease achieved in ~100 d after injection of 1×10^6 cells) and the tumorigenic, fast-developing disease representing MOSE-L_{TICv} cell lines (lethal disease achieved in 23 d after injection of 1×10^4 cells). Furthermore, since the MOSE lines express fallopian tube markers they likely represent serous ovarian cancer that can originate from the fallopian tubes and thus we used the human syngeneic benign (FNE) and malignant (FNLE) fallopian tube cell lines to confirm our data in a human model (Merritt *et al.*, 2013). Our high throughput biophysical measurements using both the MOSE model and the human syngeneic pairwise cells, all capable of being quantified in a matter of few hours, quantitate biophysical sensitivity to disease progression, thus providing both new and complementary investigative tools for early diagnosis of ovarian cancer.

RESULTS

Design of fiber networks to quantify biophysical metrics in ovarian cancer

We used the nonelectrospinning STEP technique to fabricate suspended fiber networks (Figure 1) for quantifying protrusion, *coiling*, migration dynamics, and the forces exerted by the three MOSE phenotypes representing the various stages of ovarian cancer progression.

To quantify protrusion dynamics and *coiling* occurring at the tip of the protrusion, we use an orthogonal network of fibers with mismatched fiber diameters. The larger diameter (~2000 nm) "base fibers" constrain cell migration along the base fiber axis, while orthogonally deposited smaller diameter (~500 nm) "protrusive fibers" allow the study of individual protrusions (Koons *et al.*, 2017).

To investigate cell migration, we designed fiber geometries that recapitulate the cell morphology observed in vivo in the complex, fibrous submesothelium. Transmission electron micrograph images taken in separate studies have shown stromal cells adopting a distinctly polarized and elongated morphology while interacting with collagen fibers in the submesothelium (Dobbie *et al.*, 1981; Thomas, 1987). Since these shapes are typically associated with persistent migration in cancer invasion, we used our previously described strategies of parallel networks of fibers (Sharma *et al.*, 2013; Sheets *et al.*, 2013; Estabridis *et al.*, 2018) and cross-hatch network of fibers

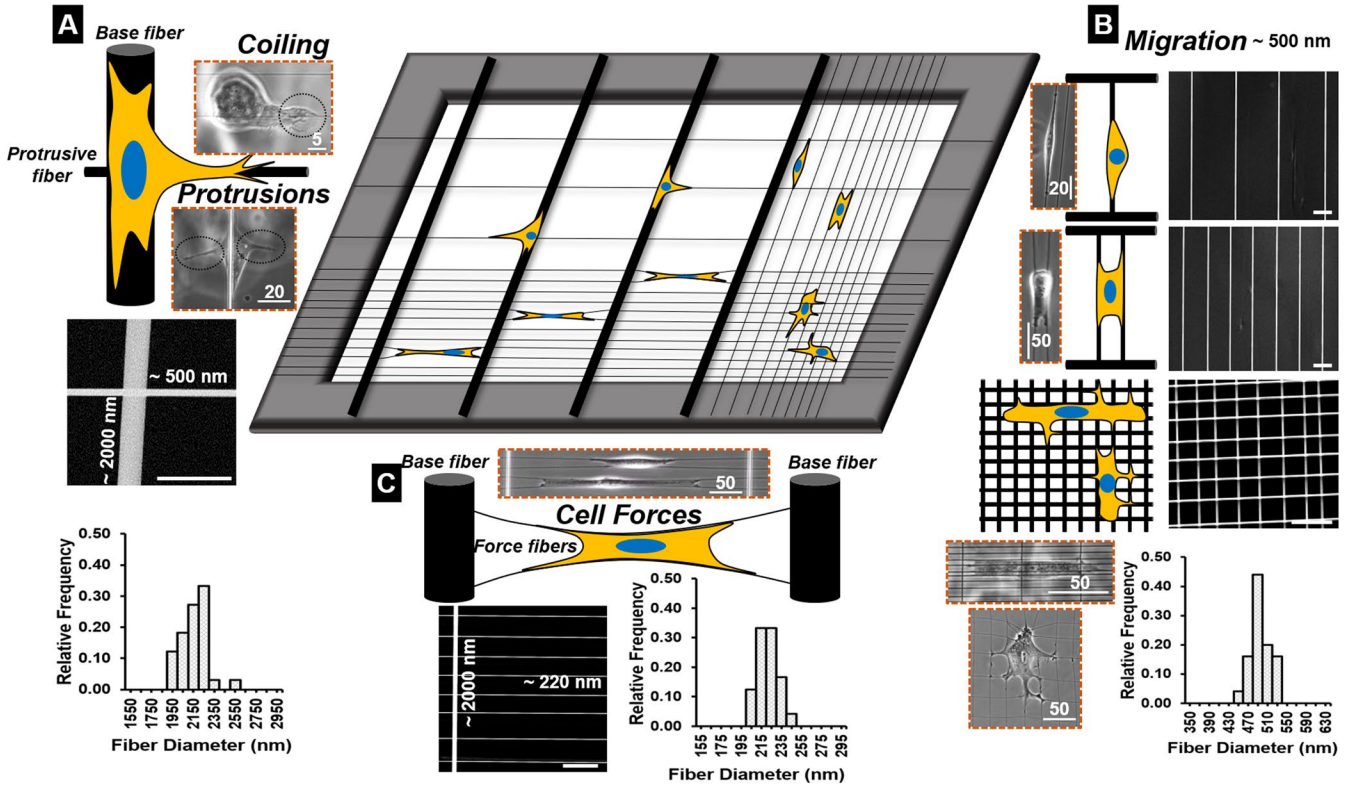

FIGURE 1: Overview of the STEP suspended fiber networks used to quantify biophysical metrics. (Center) Schematic showing an overview of the suspended fiber networks with precisely tunable network architecture. Schematic and corresponding SEM images of the specific fiber networks used to quantify (A) protrusion and *coiling* dynamics, (B) migration dynamics on single fiber, two fiber and crosshatch networks, and (C) forces exerted during migration. Histograms show the fiber diameter distribution for the ~2 μm "base fibers" used in the protrusion and force networks, ~500 nm diameter fibers used in the protrusion and migration networks and ~220 nm diameter fibers used in the force networks. Inset images in dashed boxes are representative images of associated cell behavior with numbers denoting scale bars in microns. Scale bars in all SEM images are 10 μm.

(Jana *et al.*, 2019) to achieve shape-dependent persistent migration. Specifically, modulating the spacing between adjacent aligned fibers allowed us to study cell migration in elongated shapes on "single fibers" (~25 μm interfiber spacing), on "two fibers" (~15 μm interfiber spacing), and on cross-hatch network of fibers with a ~6 μm × ~6 μm grid size.

Cells migrating in fibrous environments tug on individual fibers causing them to deform. To estimate the tugging forces, we have developed the nanonet force microscopy (NFM) technique (Sheets *et al.*, 2016; Tu-Sekine *et al.*, 2019; Padhi *et al.*, 2020a,b). Briefly, NFM nanonets are comprised of strutlike, large diameter (~2000 nm) base fibers orthogonal to which are deposited smaller diameter (~220 nm) "force fibers" (Figure 1C). NFM estimates forces from deflection of fibers and by establishing force vectors that originate from focal adhesion clustering (FAC) occurring at poles of cells and directed along the dominant tension-bearing F-actin stress fibers.

All measurements described in this study were conducted in hours using metric-specific fiber networks and can be combined in a single scaffold for high throughput and high content screening (schematic in Figure 1).

Protrusion length is the longest in the MOSE$_{TICv}$ phenotype

Cells extend protrusions to probe and sense the surrounding environment continuously. We wanted to inquire if in vitro fibrous environments can identify the metastatic potential of cancer cells through protrusion dynamics. We defined two metrics of eccentricity (E) and protrusion length (L) (Figure 2Ai) to quantify protrusion dynamics (Koons *et al.*, 2017; Mukherjee *et al.*, 2019). The eccentricity metric represents the shape of a protrusion, with low eccentricity (E< ~0.6), signifying a "rodlike" protrusion, while high eccentricity (E > ~0.8) signifies a "kite-shaped" broad protrusion. The combination of two metrics defines a "protrusion cycle" which typically lasted less than 2 h for each phenotype. The cycle started with the broadening of the protrusion (increase in E), followed by an increase in the length, and ended with protrusion retraction to the main cell body (Figure 2Aii; Supplemental Movie S1). Phase images depicting a typical protrusion cycle for each MOSE phenotype are shown in Figure 2B, while representative plots for protrusion cycles for all three phenotypes are shown in Supplemental Figure S1. We quantified both the maximum eccentricity and the maximum protrusion length for the three MOSE phenotypes (MOSE-E, MOSE-L, and MOSE-L$_{TICv}$). We found that there was no significant difference in the average maximum eccentricity (Figure 2Ci). However, the maximum protrusion length was lowest in the MOSE-L cells (19.2 ± 1.0 μm) while the MOSE-L$_{TICv}$ cells formed the longest protrusions (average length of 54.1 ± 3.4 μm; Figure 2Cii). Overall, our results indicate that the cancer phenotype representing fast-developing disease in the model correlates with the most extended protrusions.

Coiling at the tip of protrusions correlates with an increasingly aggressive MOSE phenotype

While extending protrusions, cancer cells sense the fiber curvature by *coiling* (wrapping-around the fiber axis) at the tip of the protrusion (Mukherjee *et al.*, 2019) (Supplemental Movie S2). We wanted

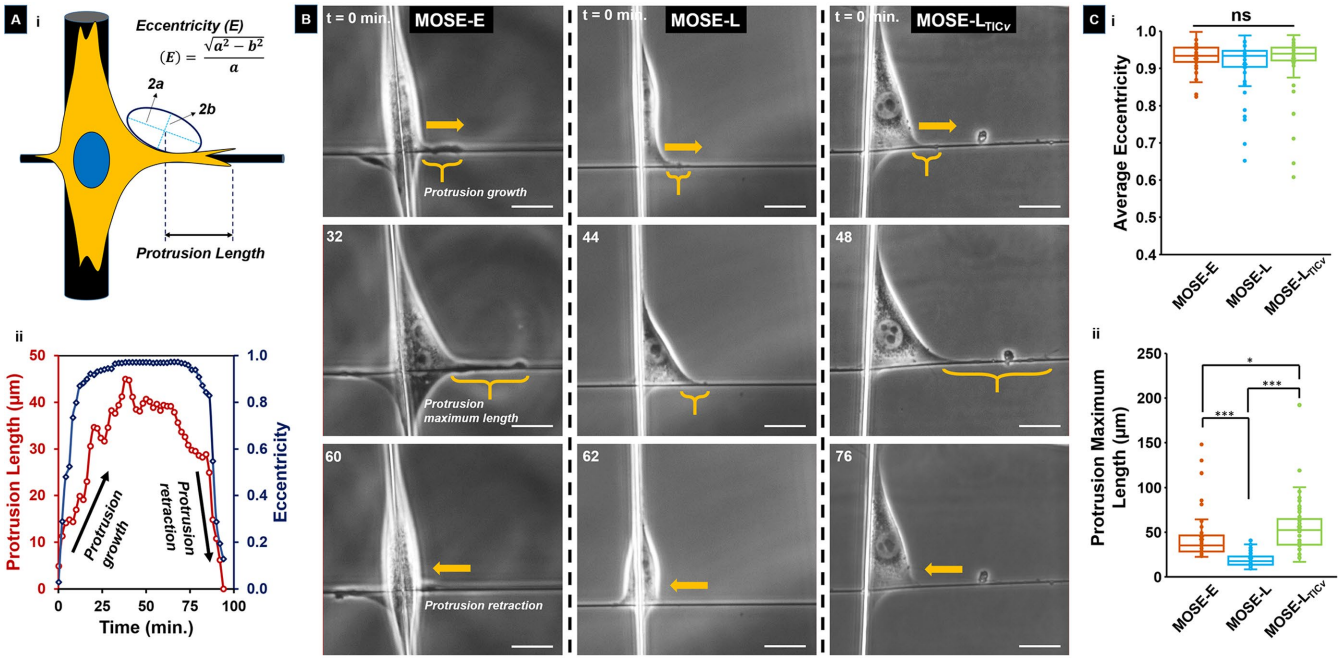

FIGURE 2: Protrusion dynamics show significant differences across the MOSE model. (A.i) Schematic showing measurements for protrusion length ("L") and eccentricity ("E"). (A.ii) Representative "protrusion cycle" plot for a MOSE-E cell. (B) Representative phase images for all three MOSE phenotypes showing typical protrusion cycles. Yellow parentheses indicate the protrusions in each image. Scale bars are all 20 μm. (C) Comparing the (i) maximum average eccentricity and (ii) maximum protrusion length for the MOSE-E, MOSE-L, and MOSE-L$_{TICV}$ cells; *n* values for the MOSE-E, MOSE-L, and MOSE-L$_{TICV}$ cells are 50 (23 cells), 55 (25 cells), and 64 (28 cells), respectively.

to inquire if *coiling* dynamics (Figure 3A) could be used as a measure of the disease progression in the MOSE model. From the *coiling* cycles for the three MOSE phenotypes (Figure 3B), we found that the maximum *coil* width increased with increasing aggressiveness of the MOSE model, with the MOSE-L$_{TICV}$ cells showing a maximum *coil* width of 3.4 ± 0.1 μm, representing a 48% increase over the maximum *coil* width of 2.3 ± 0.1 μm displayed by the benign MOSE-E cells (Figure 3Ci). Furthermore, we found that the time taken to reach the maximum width increased with the disease stage (Figure 3Cii). Thus our data of *coiling* at the tip of the protrusion show stark differences across the MOSE model and suggest its potential use as a useful biophysical metric to determine metastatic capacity.

Migration speed of polarized cells depends on cell shape and disease stage

Given that protrusive activity is widely considered a precursor to cell migration (Friedl and Wolf, 2003; Stoletov *et al.*, 2018), we investigated whether the differences in protrusive dynamics and *coiling* behavior translated to differences in migration dynamics on suspended fibers across the MOSE model. To this end, we determined polarized single-cell migration on anisotropic (single fiber and two fibers) and low interfiber spacing dense orthogonal ("cross-hatch network") networks. We used cell migration on the flat, 2D glass surface as a control (Figure 4A, i–iv). Before quantifying the migration rate, we inquired whether the cell morphology was different across the MOSE phenotypes on the different substrates as both the spread area (Webb *et al.*, 2000) and the degree of polarization (Condeelis and Segall, 2003) have previously been linked with influencing migration dynamics. Thus we quantified both the cell spread area and circularity (a circularity value close to 1 indicates a perfect circle). We found that the benign MOSE-E cells had the largest spread area, and the area decreased with an increase in invasiveness (Figure 4B, i–iv). Circularity, on the other hand, was the highest on flat 2D, indicating cells to be broad in shape (Figure 4C, i–iv). The low values of circularity indicating elongated shapes for cells on the single- and two-fiber systems were expected. However, for cells attached to single fibers (spindle-shaped cells), the intermediate phenotype (MOSE-L) unexpectedly had the lowest area and highest circularity, indicating a rounded spindle morphology. Overall, our analysis across all substrates showed that the benign cells have the most extensive areas, whereas the circularity measure was not able to distinguish shape-based differences.

Having quantified the cell morphology, we next investigated their migration dynamics (Supplemental Movies S3–S6). First, we found that MOSE cells, regardless of the phenotype, migrated faster on suspended fibers compared with flat 2D (Supplemental Figure S2). Next, we wanted to interrogate whether the faster migration rate correlated with disease progression. We found that the migration rate increased with the invasiveness of MOSE cells, except for intermediate MOSE-L cells migrating faster on single fibers (Figure 4D, i–iv). Specifically, the migration speed for the stemlike MOSE-L$_{TICV}$ cells increased by 124, 149, and 126% over those of the benign MOSE-E cells on the two-fiber, cross-hatch network, and flat substrates, respectively. Finally, we inquired if the faster migration rates observed on fibers were driven by differences in the persistence of motion for the cells. We found that on all the fiber categories, all phenotypes had higher persistence values compared with flat 2D cells. Generally, the most advanced phenotype did exhibit the highest persistence on each fiber substrate, although there was no statistical difference observed on either the single-fiber or the two-fiber networks (Figure 4E, i–iv). Altogether, our data show that the phenotype in the MOSE model that represents fast-developing disease and has stemlike properties has the lowest area but migrates the fastest with the highest persistence.

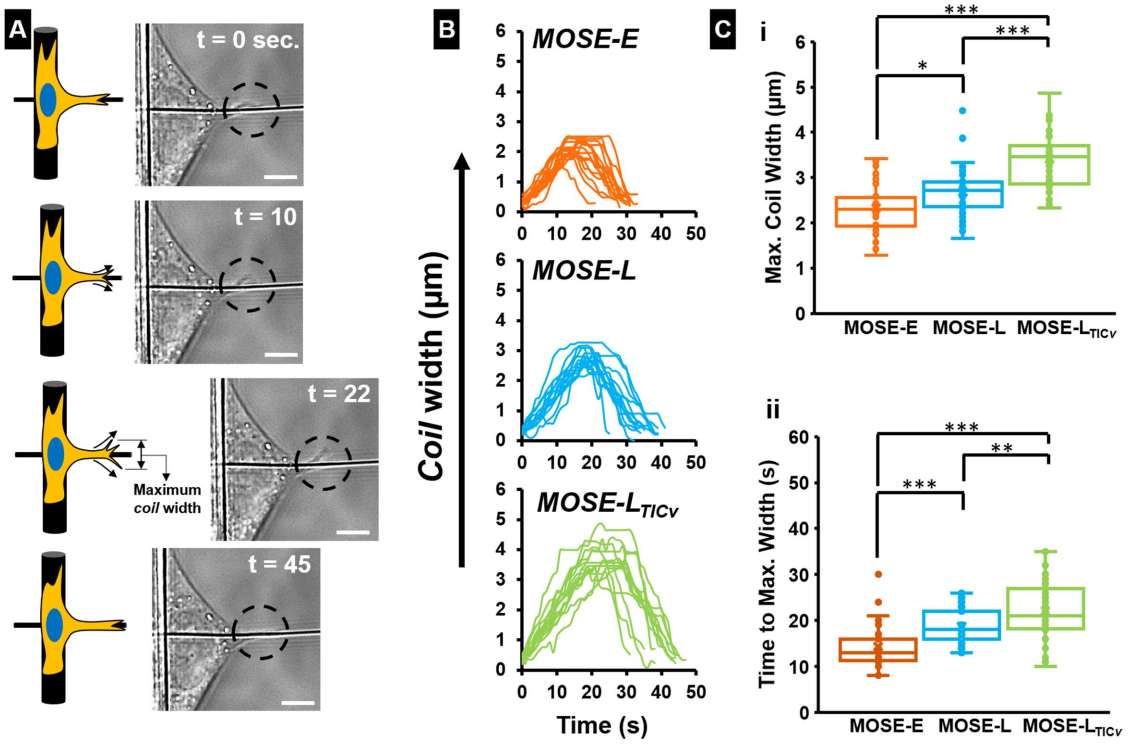

FIGURE 3: *Coiling* dynamics at the tip of the protrusion are influenced by disease progression in the MOSE model. (A) Schematic and phase images depicting a typical *coiling* cycle for a MOSE-L cell. Black dotted circles indicate the *coiling* structures. Scale bars are all 5 µm. (B) Comparing the coiling cycle between the MOSE-E, MOSE-L, and MOSE-L_{TICv}phenotypes. Sixteen *coiling* cycle profiles are shown for each case. (C) Comparing the (i) maximum *coil* width and (ii) time taken to reach the maximum *coil* width across the MOSE model; $n = 40$ for each category.

MOSE force-disease biphasic relationship exhibits F-actin network dependence

During the migration process, cells continuously generate actomyosin contractility-driven forces that act on the surrounding substrate (Gupton and Waterman-Storer, 2006). Given that the actin cytoskeleton undergoes significant reorganization during the disease progression in the MOSE model (Creekmore *et al.*, 2011), we enquired if this correlated with the forces exerted by single cells. We have previously shown that on 2D flat substrates, the benign MOSE-E cells exhibit distinct actin cables in contrast to the cancerous MOSE-L, which exhibit a dense, meshlike network lacking in prominent stress fibers (Creekmore *et al.*, 2011). We used NFM (Figure 5A) to quantify the forces by establishing force vectors that originate at FAC and are directed along the F-actin stress fibers. Using fluorescent images of filamentous actin (Figure 5Bi), we found that the average stress fiber angle of 10.2 ± 0.5 degrees in benign MOSE-E cells was significantly lower than both the MOSE-L (16.1 ± 1.4) and the MOSE-L_{TICv} (15.5 ± 0.9) cell lines. Using these average F-actin stress fiber angle values in our finite element model, we computed the forces exerted by single cells. We found that MOSE-E cells exerted the highest force of 305 ± 24 nN, which was 189 and 75% higher than the force exerted by the MOSE-L (106 ± 9 nN) and the MOSE-L_{TICv} (174 ± 10 nN) cells, respectively (Figure 5Bii; Supplemental Movies S7–S9). The highest force being exerted by the MOSE-E cells is not surprising due to these cells having prominent actin stress fibers compared with the other two aggressive cell types. This result is also consistent with the lowest migration speed of these cells (Figure 4Dii). The lower forces exerted by MOSE-L is presumably due to the loss of well-defined actin networks (Figure 5C) and the wider distribution of angles formed by F-actin stress fibers, thus causing a large variability in force values. Indeed, on quantifying the length of the actin filaments across the MOSE model, we find that the MOSE-E cells show significantly longer actin filaments on the fiber networks compared with both the aggressive phenotypes signifying a transition from a cell-spanning, well-defined network in the MOSE-E cells to the more meshlike structures composed of shorter filaments in the MOSE-L and MOSE-L_{TICv} cells (Supplemental Figure S5A). Even on the flat surface, the actin filament length decreases with increasing aggression although the results are not statistically different (Supplemental Figure S5B). The increase in forces in the MOSE-L_{TICv} may be attributable to the partial reassembly of F-actin networks (Figure 5C).

We inquired if decreased forces in aggressive phenotypes resulted in changes in nuclear morphology. We stained for the nucleus and then took z-stack slices of the nucleus using confocal microscopy to measure the thickness of the nucleus. We found that MOSE-E cells showed the most compressed nuclei while MOSE-L cells exhibited the thickest nuclei, corresponding to the highest and lowest forces exerted, respectively (Supplemental Figure S6). Previously we had shown that expression of myosin light chain kinase (MLCK) in the intermediate MOSE-L phenotype increased in comparison to the benign MOSE-E phenotype which was accompanied by an increase in the activation of phosphorylated myosin light chain (pMLC) expression driven primarily by an increase in MLCK (Creekmore *et al.*, 2013) (Supplemental Figure S7, A–D). We analyzed the most aggressive phenotype MOSE-L_{TICv} and found a reduced expression of MLCK compared with the MOSE-L but which was still higher than in the MOSE-E cells (Supplemental Figure S7E).

Finally, given that the force transduction machinery relies on focal adhesions to interact with the surrounding substrate, we

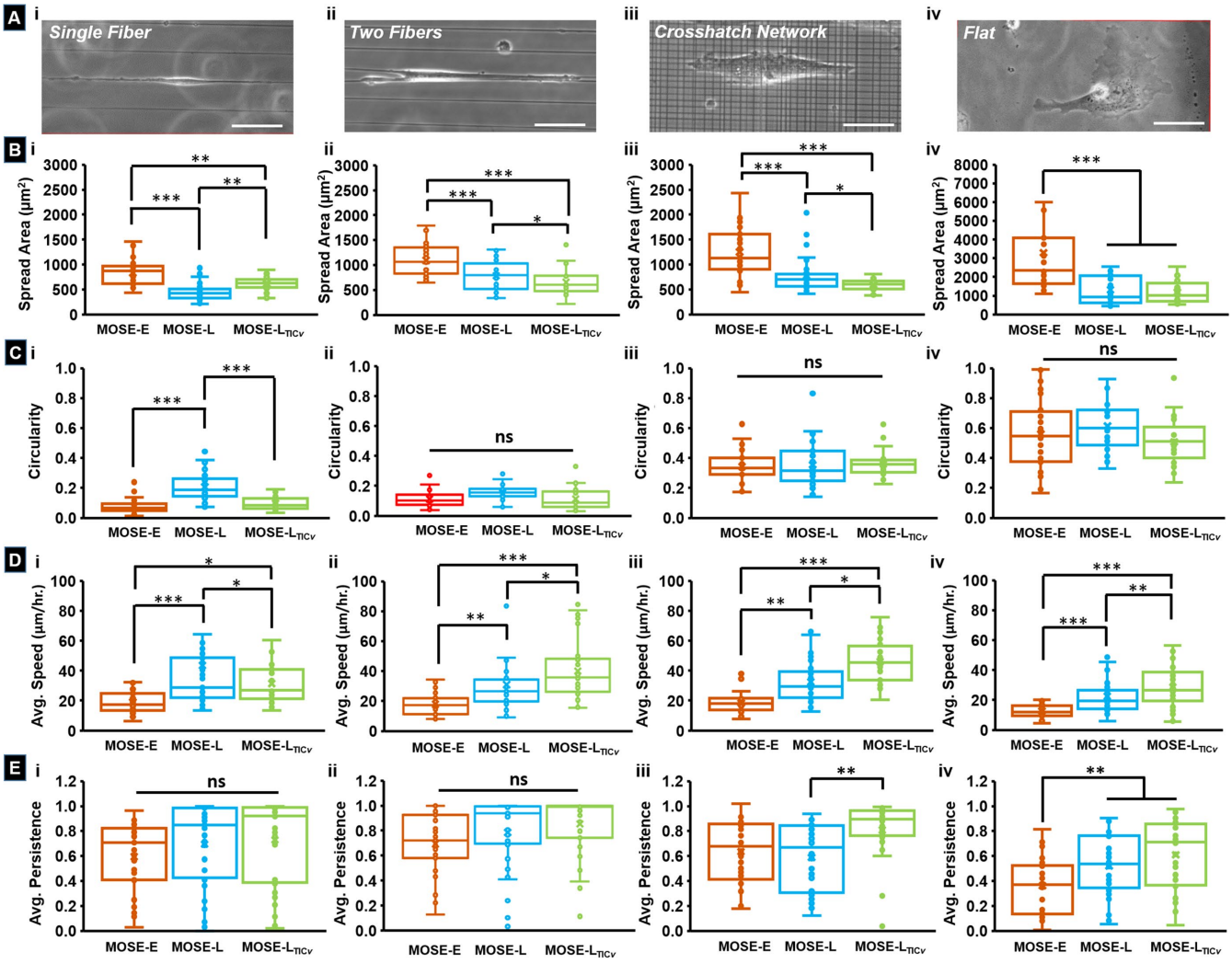

FIGURE 4: Migration of MOSE cells on suspended fiber substrates shows disease progression dependency. (A) Representative phase microscopy images showing MOSE-E cells on (i) a single fiber migration assay (cell interacting with only one fiber), (ii) a two-fiber migration assay (cell interacting with two fibers), (iii) a cross-hatch network migration assay (cell interacting with an orthogonal fiber network), and (iv) on a flat, 2D surface (control). All the scale bars are 50 μm. Comparison of the cell spread area (B), circularity (C), average migration speed (D), and average persistence (E) across the MOSE model on the (i) single fiber, (ii) two fibers, (iii) cross-hatch network, and (iv) flat substrates; $n = 35$ for all the single fiber substrates (MOSE-E, MOSE-L, and MOSE-L$_{TICV}$), 30 for all the two fiber substrates, 32 for the cross-hatch network, and 25 for the flat surface.

quantified the focal adhesion pattern across the MOSE model. On staining for adhesion protein paxillin, we found that both aggressive phenotypes exhibit significantly shorter focal adhesions in comparison to the benign MOSE-E phenotype. However, there are no significant differences between the two aggressive phenotypes (Supplemental Figure S8).

Taken together, our results suggest that with disease progression, cancer cells exert lower forces compared with benign cells, which is influenced by the length network of F-actin stress fibers, increased MLCK expression, and a reduction in the size of focal adhesions.

Human ovarian cancer cell pair shows similar biophysical trends as the MOSE Model

We next wanted to confirm that the biophysical metrics for the MOSE cells, a model for serous ovarian cancer, were not limited to a mouse cell model but could be extended to human cancer cell lines. To this end, we repeated key protrusion, *coiling*, force, and migration measurements for benign (FNE) and malignant (FNLE) human fallopian tube cancer cells; the aggressive phenotype of these cells is not available. Overall, we found that the FNE/FNLE cell pair followed the same trend as observed between the MOSE-E (benign) and the MOSE-L (slow developing disease) cells in the MOSE model. Specifically, the FNE cells exhibited longer protrusion length (Figure 6Ai; Supplemental Movies S10 and S11) and lower maximum *coil* width compared with the transformed FNLE counterparts (Figure 6Aii; Supplemental Movies S12 and S13). Furthermore, on using NFM to quantify the forces exerted by single cells, we found that the FNE cells exerted significantly larger forces on the suspended fibers compared with the FNLE cells (Supplemental Movies S14 and S15) that may be correlated to their extensive actin stress fibers (Supplemental Figure S4) and the lower stress fiber angle indicating a more contractile morphology (Figure 6B, i and ii). Finally, quantification of the migration dynamics on single fiber

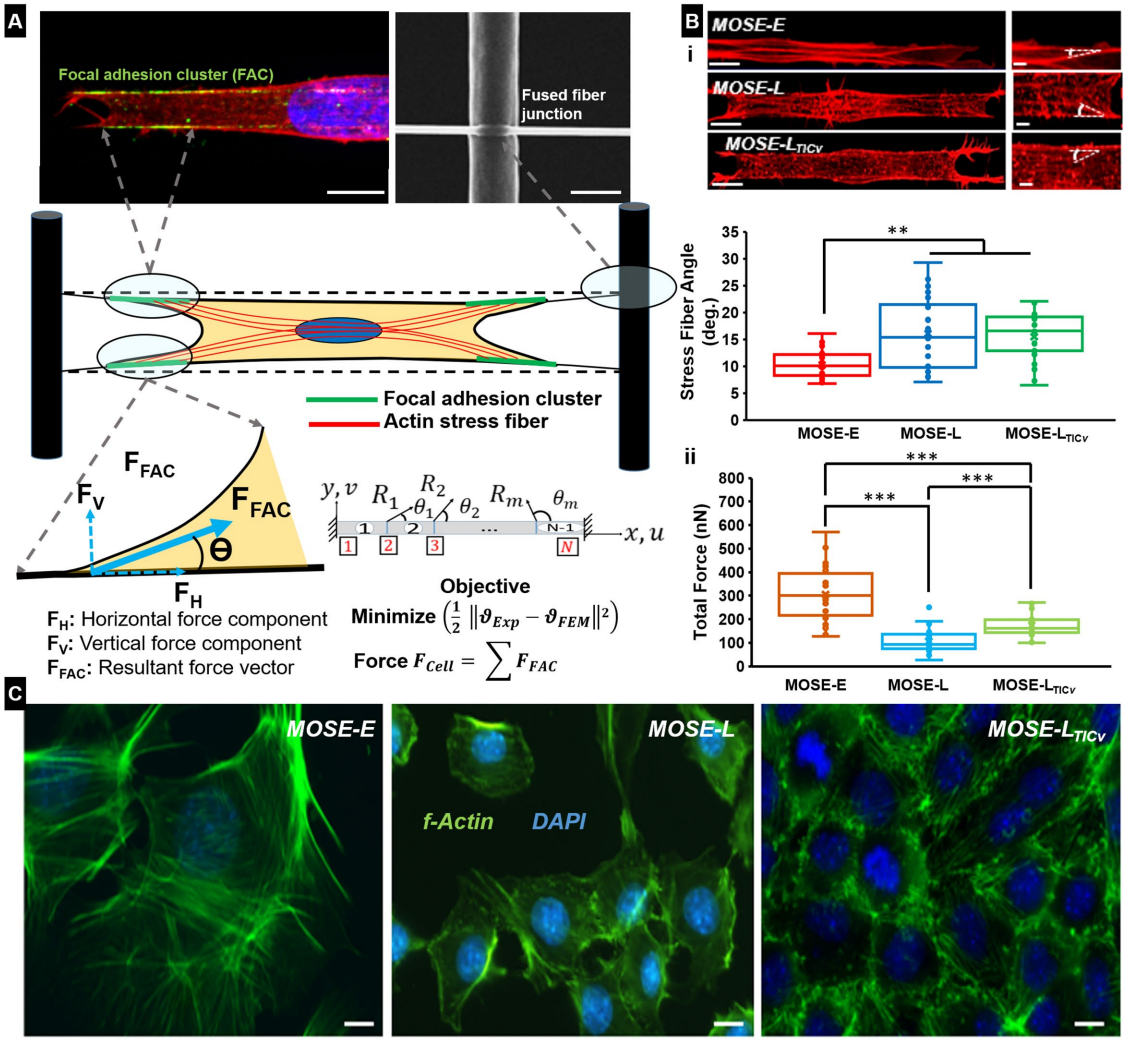

FIGURE 5: Quantifying forces exerted by the MOSE model using NFM. (A) Schematic providing an overview of how forces are calculated using NFM. The fluorescent image on the top left shows actin filaments in red, nucleus in blue and paxillin in green. The SEM image shows a fused fiber junction. Scale bar is 10 μm in the fluorescent image and 2 μm in the SEM image. (B) Representative fluorescence microscopy images of (i) MOSE-E, MOSE-L, and MOSE-L_{TICv} cells with F-actin stained in red. To the right of each image is a zoomed in region highlighting the stress fiber angle (the angle is shown by the white dotted lines). The scale bars are 10 and 5 μm for the fluorescent images and their corresponding enlarged images, respectively. Quantifying the (ii) average stress fiber angle and (iii) force exerted across the MOSE cell lines; $n = 27$, 22, and 23 for the stress fiber angle measurements for the MOSE-E, MOSE-L, and MOSE-L_{TICv} cells, respectively; $n = 24$, 30, and 27 for the force measurements for the MOSE-E, MOSE-L, and MOSE-L_{TICv} cells, respectively. (C) Representative immunofluorescence images of F-actin stress fiber networks in cells on flat 2D showing well-organized actin cables in benign cells, loss, and partial recovery of F-actin structures in intermediate and aggressive phenotypes, respectively. Scale bars 10 μm.

networks, two fiber networks, and on flat (which served as the control) revealed that the FNLE cells migrated faster on all substrates compared with the FNE cells (Figure 6C; Supplemental Movies S16 and S17), similar to the trend observed between the MOSE-L cells as compared with the MOSE-E cells in the mouse model. The higher speed observed for the FNLE cells was driven by a higher persistence on both fiber networks and the flat surface (Figure 6D).

In addition to the FNE and FNLE human ovarian cancer cell pair, we found that three other human ovarian cancer cell lines that we tested, A2780, Caov3, and C200, also exhibited protrusive behavior and exerted contractile forces on suspended fiber networks (Supplemental Figure S9). While these additional cell lines do not represent benign-metastatic pairwise comparisons, they further highlight that the ability of ovarian cancer cells to extend protrusions on suspended fibers and tug on them to exert contractile forces is not limited to the mouse model but is exhibited across a wide range of human ovarian cancer cell lines.

Taken together, these results indicate that the biophysical metrics described in this study are comparable to the differences between benign MOSE-E and malignant MOSE-L cells.

DISCUSSION

Despite metastasis being the leading contributor to cancer-related deaths, there is currently no clear indicator for predicting the metastatic potential of a tumor in a patient (Meirson *et al.*, 2020a). Clinical oncologists primarily depend on a combination of pathology results (Steeg, 2006; Valastyan and Weinberg, 2011) and gene expression or mutational signatures as a predictive tool for accurate

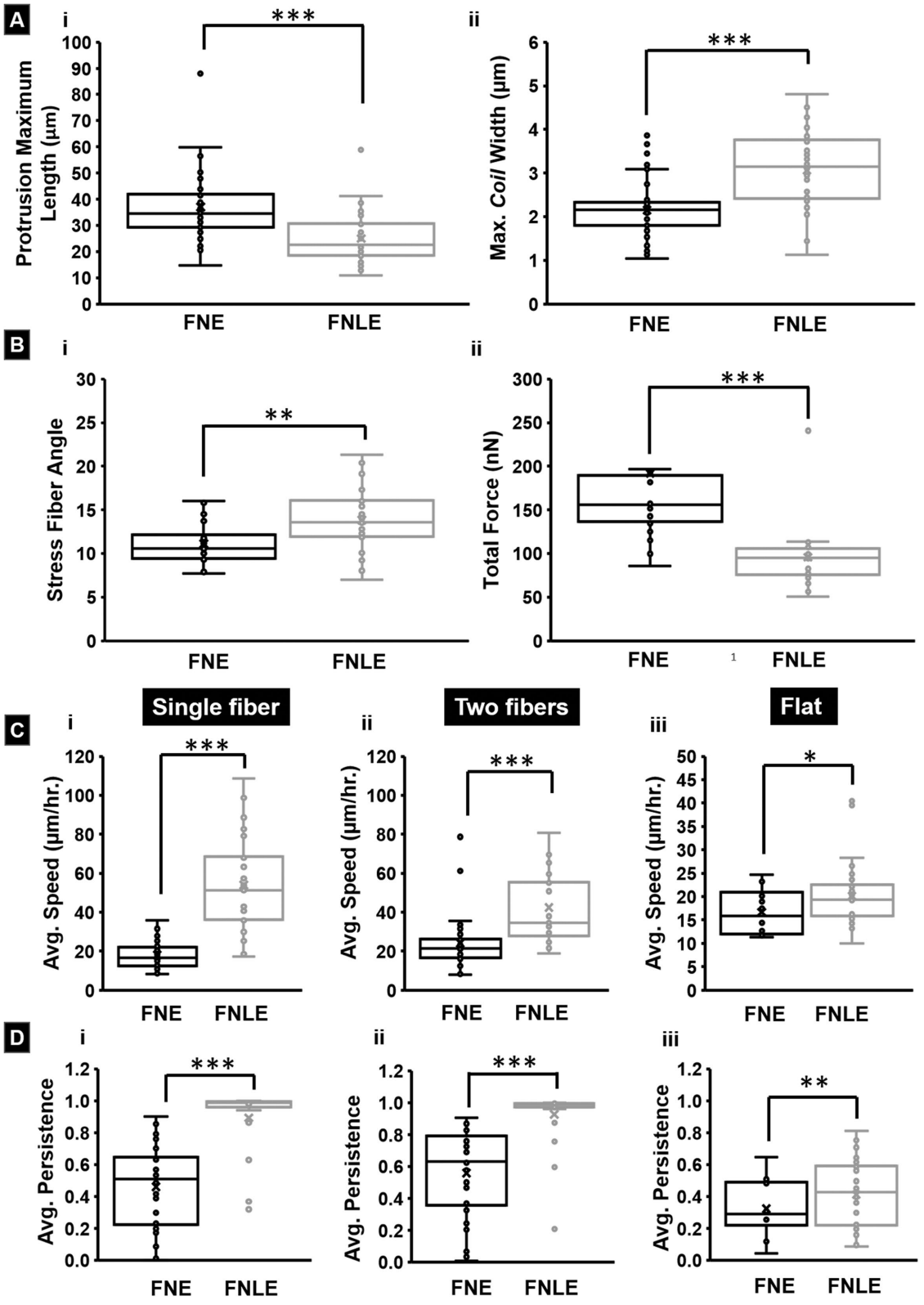

FIGURE 6: Quantification of key biophysical metrics between benign (FNE) and metastatic (FNLE) human ovarian cancer cell pair. (A) Quantification of the (i) maximum protrusion length and (ii) maximum *coil* width between the FNE and FNLE cells; *n* value is 52 for the protrusion measurements and 40 for the *coil* width measurements for each category. (B) Quantification of the (i) average stress fiber angle exhibited and (ii) the total force exerted by FNE and FNLE cells; *n* value is 28 for the stress fiber measurements and 20 for the force measurements for each cell category. Quantification of (C) migration speed and (D) persistence for both cell types on (i) single fibers, (ii) two fibers, and (iii) flat surface; *n* value is 30 and 25 for the FNE and FNLE cells, respectively, on all the substrates considered.

cancer prognosis (Hanahan and Weinberg, 2011; Garraway and Lander, 2013; Weinstein *et al.*, 2013; Lawrence *et al.*, 2014). However, genetic profiling can be a time-limiting step which is further compounded with heterogeneity in tumor populations (El-Deiry *et al.*, 2019; Wu *et al.*, 2020) and nonmutational regulatory factors that combine to determine the metastatic capacities of the cells usefully. In addition to characterizing individual genetic modifications, biophysical metrics can serve as complementary clinical indicators of metastatic potential (Kraning-Rush *et al.*, 2012).

The biophysical metrics implicated in invasion (protrusions, migration, and exertion of force) are specifically contextual in ovarian cancer metastasis due to the ability of ovarian cancer cells to physically invade through both the mesothelial layer lining the peritoneal organs and subsequently the complex fibrous submesothelium for successful dissemination to distal sites and further colonization (Tomar *et al.*, 2018). In this study, our goal was to use suspended ECM-mimicking nanofiber networks to quantify, within a timespan of hours, relevant biophysical metrics in a progressive ovarian cancer model (MOSE) to discern disease progression.

We quantitated protrusion dynamics (length and eccentricity) for the MOSE model (Figure 2) and found that the MOSE-L_{TICv} (representing advanced, fast-developing disease) formed the longest protrusions. Our findings are in agreement with our previous study that demonstrated that the highly metastatic breast adenocarcinoma MDA-MB-231 cells exhibit significantly longer protrusion lengths compared with the nontumorigenic breast epithelial MCF-10A cells (Koons *et al.*, 2017). Our findings are also in agreement with other studies using a combination of both flat 2D assays and gel-based 3D assays demonstrating that protrusions of squamous cell carcinoma, glioblastoma, bladder cancer, and breast cancer can be correlated to metastatic capacity (Coopman *et al.*, 1998; Yamamoto *et al.*, 2011; Meirson *et al.*, 2020b). However, our finding that MOSE-L phenotype extends shorter protrusions compared with the benign MOSE-E cells is unexpected. We inquired if the cell area played a role in the formation of shorter protrusions. We quantified the area of MOSE-L cells attached to the main *base* fiber in protrusion assay and found it to be significantly smaller compared with MOSE-E cells. Normalizing the protrusion length to the cell spread area did not show differences in the protrusion lengths between the benign and the intermediate cells in the MOSE model (Supplemental Figure S3). Areal normalization of the MOSE model suggests that protrusion length may not be a sufficient standalone metric capable of differentiating between benign and tumorigenic phenotypes.

Next, since *coiling* occurs at the tip of protrusions, we found that the *coil* size increased with increasing disease state of the MOSE cells independent of the cell area (Figure 3). Our findings concur with our earlier study wherein we demonstrated that the metastatic breast cancer cells exhibit significantly larger *coil* sizes compared with their nontumorigenic counterparts across a range of fiber diameters from ~135 to ~1000 nm (Mukherjee *et al.*, 2019). Altogether, our results indicate that *coiling* behavior which is unique to fiber networks correlates robustly with ovarian cancer disease progression, thus functioning as a more deterministic metric in identifying the metastatic potential of single cancer cells.

In addition to protrusion and *coiling*, we investigated cell migration as another potential biophysical marker. We designed our fiber networks to achieve in vivo resembling elongated cell morphologies that led cells of all phenotypes to move persistently compared with flat surfaces. We found that on both two-fiber and cross-hatch fiber geometries, the migration rate of the polarized ovarian cancer cells positively correlated with increasing disease state. In contrast, only in the case of the single fiber geometry the MOSE-L cells exhibited the highest migration rate, which is consistent with their smaller size and rounded spindle morphology (Figure 4). Our migration findings are in agreement with reported studies that show increasing invasive potential of cancer cells correlates with increasing migration rate across a range of cell types, including breast and thyroid cancer cells (Liu *et al.*, 2008; Papageorgis *et al.*, 2010; Ning *et al.*, 2011). Additionally, in vivo, human epidermoid cancer cells with lower invasive capacity are shown to have an approximately fourfold reduction in migration rate compared with their more invasive counterparts (Zijlstra *et al.*, 2008). Thus altogether, we suggest that migration and persistence of migration can be suitable predictors of invasive potential.

Finally, we used the NFM platform to quantify the forces exerted by the MOSE cells and found a biphasic relationship between the force exerted with disease progression such that the benign MOSE-E cells exerted the highest forces (Figure 5). While the relationship between higher migration rates and lower force exertion by aggressive cancer cells seems reasonable, previously reported studies using traction force microscopy had shown both similar and contrasting results. Our findings are in agreement with Indra *et al.* (2011), who quantified a decrease in traction forces exerted by four murine breast cancer cell lines derived from the same primary tumor but with increasing metastatic capacity (Indra *et al.*, 2011). They attributed the loss in forces to a reduction in the number of focal adhesions suggesting a less adhesion-dependent migratory mode with disease progression. In contrast, Rösel *et al.* found that metastatic A3 sarcoma cells exert five times higher traction forces compared with less metastatic K2 counterparts due to an up-regulation of ROCK protein, which promotes cytoskeletal contractility (Rösel *et al.*, 2008). Similarly, Kraning-Rush *et al.* quantified traction forces using an isogenic cell model, which represents the full spectrum of neoplastic progression in breast cancer and found that forces increased with disease progression (Kraning-Rush *et al.*, 2012). In our case, we suggest that the drop in forces with disease progression is due to the disorganization and transition of long and distinct F-actin fibers in the benign MOSE-E cells to a meshlike network in the MOSE-L cells causing them to be softer (Creekmore *et al.*, 2011; Ketene *et al.*, 2012a,b). Indeed, the angles formed by actin stress fibers are at a shallower angle in MOSE-E cells due to which these cells can apply large forces and cause the fibers to deflect more inward (Supplemental Figure S10). However, MOSE-L_{TICv} exhibit partial reassembly of actin cables compared with the MOSE-L and thus the exerted forces were higher but not reaching the levels exerted by the MOSE-E. Our data indicate that while forces are lower in ovarian cancer cells compared with the benign counterparts, the force exertion increases with invasiveness between the two cancer phenotypes. To generate the contractility required to transmit the forces, the cell relies on phosphorylation of pMLC by the MLCK (Amano *et al.*, 1996; Asokan *et al.*, 2014). Combining results from our previous work with new experiments, we report here that MLCK, myosin light chain, and the pMLC expression are all increased in the two metastatic phenotypes compared with the benign phenotype (Creekmore *et al.*, 2013). This result is also in general agreement with work from others which showed that chemoresistant ovarian cancer cell variants showed increased pMLC expression compared with drug-sensitive control cells (Kapoor *et al.*, 2018). Given that the forces exerted by the MOSE cells on our NFM platform show a marked decrease for the two metastatic phenotypes compared with the benign phenotype, it suggests that the effect of the decrease in prominent, thick actin cables with increasing aggressiveness has a more significant influence in mediating force expression than the increase in myosin expression. Finally, focal adhesions at the cell

membrane serve to transmit the internally generated forces to the external ECM. Our staining and associated quantification of FAC lengths show that the size of the clusters decreases with increasing aggression in the MOSE model. This result is in accordance with previous work by us showing that the size of focal adhesions reduced with increasing aggression in the MOSE model (Creekmore *et al.*, 2013) and others showing that focal adhesions were significantly impaired in chemoresistant ovarian cancer cells compared with their drug-sensitive control counterparts (Kapoor *et al.*, 2018). This impairment in focal adhesion distribution suggests a potential switch from mesenchymal to ameboid migration with progression in the MOSE model which is further supported by the significant increase in migration speed (Figure 4). Altogether, our findings suggest that forces can provide insights into the metastatic capacity of cancer cells.

There has always been a healthy skepticism surrounding the translational capacity of purely animal-based models to human cell lines and ultimately human subjects, stemming primarily from genomic differences between animal species and humans (Martić-Kehl *et al.*, 2012; Barré-Sinoussi and Montagutelli, 2015). To preemptively address this question in our study, we interrogated whether the biophysical trends we observed in the syngeneic mouse model were consistent in a syngeneic human ovarian cancer model comprised of FNE (benign) and FNLE (malignant) cells. Here we found that all the key biophysical metrics we quantified including protrusive behavior, *coiling* at the protrusion tip, migration dynamics, and forces exerted showed similar trends in the syngeneic human model as they did in the mouse model, providing further validation of the potential of these biophysical metrics in predicting disease progression. In addition to the conservation of the biophysical trends, previous work by us has also shown that transformation from benign to malignant phenotypes in both the MOSE model and the human FNE/FNLE cell pair lead to similar loss of filamentous mitochondria and the appearance of more locally aggregated mitochondrial structures in the perinuclear region (Greico *et al.*, 2021; Compton *et al.*, 2021).

In conclusion, by using suspended extracellular mimicking fibers, we demonstrate, within hours, high throughput and high content biophysical quantitation of key biophysical metrics across the ovarian cancer MOSE model. Suspended fibers overcome the shortcomings of flat 2D substrates, and having controlled and repeatable networks provide precise quantitation of biophysical metrics in single cells that would be challenging in 3D gels. While the biophysical behaviors (protrusion, migration, and force exertion) are shown by other methods to identify metastatic potential, we emphasize the need to study them using fiber networks, as they are sensitive to both the size and the stiffness of suspended fibers (Papageorgis *et al.*, 2010; Indra *et al.*, 2011; Sharma *et al.*, 2013; Leong *et al.*, 2014; Meehan and Nain, 2014; Hall *et al.*, 2017; Stoletov *et al.*, 2018). Our finding that the *coiling* metric, a behavior unique to fibers, is a robust metric capable of identifying metastatic potential further highlights the importance in the use of fibers to study cell behaviors. We caution that our inferences on metastatic potential are derived from a well-defined MOSE mouse model, and they need to be verified in primary human patient cells. Furthermore, the biophysical metrics by themselves may not be sufficient to describe the metastatic potential, and they should be complementarily evaluated with current diagnostic assays to understand the mechanical plasticity of cancer cells with disease progression. However, our demonstration of the importance of ECM-mimicking suspended fibers suggests the possibility of their use as natural culture environments postbiopsy, thus minimizing phenotypic shifts. Overall, the ability to quantitate phenotype-sensitive biophysical metrics within a short time span of hours provides new prescreening tools that open unique opportunities for faster detection of cancer.

METHODS

Request a protocol through *Bio-protocol*.

Fiber network manufacturing using the STEP platform

The previously reported nonelectrospinning STEP method (Nain *et al.*, 2009) was used to fabricate the suspended fiber scaffolds used in this study (Figure 1). Briefly, polystyrene (PS, Scientific Polymer Products, Ontario, NY) of ~2×10^6 g/mol molecular weight was dissolved in a 1:1 xylene:dimethylformamide (Fischer Scientific, Pittsburgh, PA) solution at 10% (wt/wt) concentration to prepare the polymer solution for spinning the ~2 µm base fibers for both the protrusion and the force studies. To spin the ~500 nm diameter fibers for the migration and protrusion studies, a 10% (wt/wt) concentration solution of ~2×10^6 g/mol molecular weight polystyrene dissolved in xylene was used. Finally, to spin the ~220 nm diameter fibers for the force studies, a 7% (wt/wt) concentration solution of ~2×10^6 g/mol molecular weight polystyrene dissolved in xylene was used. The solutions were prepared at least 2 wk prior to spinning the fibers.

Scanning electron microscopy

An environmental scanning electron microscope (ESEM) was used to take images of the suspended fibers in order to confirm the fiber diameter. Prior to imaging the scaffolds, they were coated with a 7 nm-thick layer of platinum-palladium using a Leica sputter coater (Leica, Wetzlar, Germany). The images were taken at an electron beam voltage of 10 kV and a spot size of 3.5 using the ETD detector. The working distance was maintained at ~11 mm. Appropriate magnification was used depending on the application.

Cell culture

MOSE cell lines representing benign (MOSE-E), slow-developing (MOSE-L), and fast-developing disease (MOSE-L_{TICV}) of ovarian cancer generated from C57BL/6 mice have been extensively characterized previously (Roberts *et al.*, 2005; Creekmore *et al.*, 2011; Anderson *et al.*, 2013; Cohen *et al.*, 2013). MOSE cells were cultured in high glucose DMEM (Sigma-Aldrich) supplemented with 4% fetal bovine serum (Atlanta Biological), 3.7 g/l sodium bicarbonate, and 10 ml/l of penicillin-streptomycin solution with a pH of 7.4 at 37°C in 5% CO_2 in humidified conditions (Merritt *et al.*, 2013). The human syngeneic benign (FNE) and malignant (FNLE) fallopian tube cell lines were both obtained from the Miami Sylvester Comprehensive Cancer Center. These cells were cultured in Primaria tissue culture flasks (Becton Dickinson) with FOMI medium (Sylvester Cancer Center) supplemented with 25 ng/ml cholera toxin (Sigma) as described (Merritt *et al.*, 2013). The A2780 cells were cultured in RPMI 1640 medium (Thermo Fisher Scientific) supplemented with 10% fetal bovine serum, 1% penicillin-streptomycin, 2% L-glutamine, and 0.002% plasmocin. The C200 cells were cultured in RPMI 1640 medium (Thermo Fisher Scientific) supplemented with 10% fetal bovine serum, 1% penicillin-streptomycin, 2% L-glutamine, 0.00025% insulin, and 0.002% plasmocin. The Caov-3 cells were cultured in DMEM medium (Thermo Fisher Scientific) supplemented with 10% fetal bovine serum, 1% penicillin-streptomycin, and 0.002% plasmocin.

Cell seeding and experiment

To prepare for the experiments, the scaffolds were first fixed to the glass bottom of 6-well dishes (MatTek Corp., Ashland, MA) using

sterile, high-vacuum grease (Dow Corning, Midland, MI). Next, each well was filled with 2 ml of 70% ethanol in order to disinfect the scaffolds followed by two phosphate-buffered saline (PBS) rinses (Thermo Fisher Scientific). Subsequently, the fibers were coated with 4 µg/ml fibronectin (Invitrogen, Carsbad, CA) for 2 h prior to cell seeding to aid cell attachment to the fibers. Once the cell culture reached ~80% confluency, 0.25% trypsin (ATCC, Manassas, VA) was added and the culture was incubated for ~1 min. Following the incubation, 5 ml of fresh cell media were added to inhibit the effect of the trypsin. Finally, cells were seeded at a density of ~300,000 cells/ml on the scaffolds and were allowed to attach to the fibers for ~3 h. Once the cells had attached to the fibers, 3 ml of media were added to each well.

Microscopy and imaging

The cells were imaged using the AxioObserver Z.1 (with mRm camera) microscope (Carl Zeiss, Germany) at 20× magnification for the protrusion, migration, and force studies and at 63× (water immersion objective) magnification for the *coiling* studies. The cells were imaged at intervals of 4 min for the migration studies, 3 min for the force studies, 2 min for the protrusion studies, and 1 s for the *coiling* studies. All the videos were analyzed using ImageJ (National Institutes of Health, Bethesda, MD).

Analysis of biophysical metrics

For the protrusion analysis, the maximum protrusion length was calculated as previously described (Koons *et al.*, 2017). Briefly, first the distance from the base fiber to the protrusion tip was measured (L_b). Next, the largest possible ellipse was fit along the curvature of the protrusion such that one end of the ellipse was located on the protrusion at a distance of $0.8 \times L_b$ from the base fiber. Finally, the protrusion length (L) was measured as the distance from the tip of the protrusion to the projection of the intersection of the major and minor axes of this ellipse with the protrusive fiber. The eccentricity of the protrusion (E) was calculated as follows:

$$Eccentricity = \frac{\sqrt{a^2 - b^2}}{a}$$

where a and b are the semimajor and semiminor axis, respectively, of the ellipse fit to the protrusion as described in Figure 2A.

The *coiling* dynamics at the tip of the protrusion were calculated as previously described (Mukherjee *et al.*, 2019). Briefly, the maximum *coil* width (Figure 3A) was calculated as the largest *coil* width during a *coiling* cycle. The time taken to reach maximum *coil* width was calculated as the total time taken from the initiation of a *coiling* cycle until the maximum *coil* width was reached.

For the migration analysis, cells were manually tracked using ImageJ, and the x,y location of the cell centroid was recorded for every third frame (i.e., every 12 min). The instantaneous speed was then calculated as follows (in µm/h):

$$Instantaneous\ Speed = \frac{\sqrt{(y_t - y_{t-1})^2 + (x_t - x_{t-1})^2} \times 60}{12}$$

where (x_{t-1}, y_{t-1}) are the coordinates of the centroid of a cell at any given frame in µm while (x_t, y_t) are the coordinates of the centroid of the same cell three frames (i.e., 12 min) later. The overall average speed of the cell was then calculated as the average of all the instantaneous speed values. The persistence of migration was calculated as follows:

$$Persistence = \frac{\sqrt{(y_{final} - y_{initial})^2 + (x_{final} - x_{initial})^2}}{\sum_{t=1}^{t=n} \sqrt{(y_t - y_{t-1})^2 + (x_t - x_{t-1})^2}}$$

where (x_{final}, y_{final}) are the coordinates of the centroid of a cell at the last frame (nth frame) tracked in µm while ($x_{initial}$, $y_{initial}$) are the coordinates of the centroid of the same cell at the first frame tracked. The denominator is defined similar as that above for the instantaneous speed.

The circularity of the cell during migration was defined as follows:

$$Circularity = \frac{4 \times \pi \times Cell\ Area}{(Cell\ Perimeter)^2}$$

The value for circularity ranges from 0 to 1 wherein a value closer to 1 indicates a circular shape while a value closer to 0 indicates a "straight-line" shape. To quantify the average circularity and average spread area of the cell during migration, three random frames were chosen, and both these metrics were averaged over these three frames.

The analysis of the fluorescent actin channel for actin filament length measurement was done using the Filament Sensor 2.0 from the SFB 755 project (Hauke *et al.*, 2021). The datasets obtained were then organized, plotted, and statistically analyzed using RStudio Build 351 with R version 4.1.1.

For the analysis, cells that were in contact with another cell or dividing during the imaging window were not considered. All measurements were taken from multiple, independent experimental rounds.

Force model for NFM

To calculate the forces from the fiber deflections, the fiber deflection was tracked for three randomly selected, consecutive frames and was analyzed in MATLAB (2017a) using our previously reported methods (Sheets *et al.*, 2016; Tu-Sekine *et al.*, 2019). Briefly, the ~220 nm diameter, horizontal force fibers were modeled as beams with fixed-fixed boundary conditions since they were fused to the larger diameter ~2 µm, vertical base fibers at both ends (Figure 5A). A finite element model was used to obtain the fiber deflection profile from an arbitrary initial force input and the error between the model fiber profile and the experimentally tracked profile was minimized by using an optimization framework while simultaneously updating the force values iteratively (Figure 5A). The average force was finally calculated as the average of the three consecutive frames selected.

Immunostaining and Western blot

Cells were fixed in 4% paraformaldehyde (Santa Cruz Biotechnology, Dallas, Texas) dissolved in PBS for 15 min, and rinsed in PBS twice. The cells were then permeabilized with 300 µl permeabilization solution (0.1% Triton X-100 in PBS). After 15 min, the cells were blocked by 10% goat serum in PBS for 30 min and incubated with the anti-paxillin antibody (Invitrogen, Carlsbad, CA) in antibody dilution buffer (0.3% Triton X-100 and 1% bovine serum albumin in PBS) at a ratio of 1:100 overnight at 4°C. The secondary antibody Alexa Fluor 488 goat anti-rabbit (Invitrogen) and the rhodamine– or FITC–conjugated phalloidin were diluted in the antibody dilution buffer at the ratio of 1:100 and 1:80, respectively, and added to the wells. The sample was then stored in a dark place for 45 min followed by three PBS washes. Finally, the nuclei were counterstained with 300 nM of DAPI (Invitrogen) for 15 min. The scaffolds were kept

hydrated in 2 ml of PBS and imaged using a 63× (water-based immersion) magnification.

Cells were grown on tissue culture plates for 3 d. The cells were scraped and proteins were lysed in RIPA buffer. Western blotting was performed as described and probed for MLCK (Sigma-Aldrich) and normalized to total protein (Fisher Scientific) (Compton *et al.*, 2021).

Statistics

Statistical analysis of the data was conducted using RStudio (RStudio, Boston, MA) software. The Shapiro–Wilks normality test was used to check the normality of the datasets. Analysis of variance (ANOVA) was used to test for the statistical significance between different datasets. The following symbols are used to represent the statistical significance levels: *< 0.05, **< 0.01, and ***< 0.001. If there is no comparison shown between any datasets, it implies that there is no statistically significant difference between them. All error bars represent standard error of mean.

ACKNOWLEDGMENTS

This work is partially supported by the National Science Foundation awarded to A.S.N. (1762634). B.B. acknowledges partial support from the National Science Foundation (CAREER award, CBET-1454226). A.S.N., B.B., and ES acknowledge the Institute of Critical Technologies and Sciences (ICTAS) and the Macromolecules Innovative Institute at Virginia Tech for their support in conducting this study. A.M. and A.S.N. thank members of the STEP Lab for their helpful suggestions and discussions. A.S.N. dedicates this manuscript to the memory of Dolly Batra Kapahi and others who courageously fought ovarian cancer.

REFERENCES

Alkmin S, Brodziski R, Simon H, Hinton D, Goldsmith RH, Patankar M, Campagnola PJ (2020). Role of collagen fiber morphology on ovarian cancer cell migration using image-based models of the extracellular matrix. Cancers 12, 1–9.

Amano M, Ito M, Kimura K, Fukata Y, Chihara K, Nakano T, Matsuura Y, Kaibuchi K (1996). Phosphorylation and activation of myosin by Rho-associated kinase (Rho-kinase). J Biol Chem 271, 20246–20249.

Anderson AS, Roberts PC, Frisard MI, McMillan RP, Brown TJ, Lawless MH, Hulver MW, Schmelz EM (2013). Metabolic changes during ovarian cancer progression as targets for sphingosine treatment. Exp Cell Res 319, 1431–1442.

Asokan SB, Johnson HE, Rahman A, King SJ, Rotty JD, Lebedeva IP, Haugh JM, Bear JE (2014). Mesenchymal Chemotaxis Requires Selective Inactivation of Myosin II at the Leading Edge via a Noncanonical PLCγ/PKCα Pathway. Developmental Cell 31, 747–760.

El Aziz MAA, Agarwal K, Dasari S, Mitra AK (2019). Productive cross-talk with the microenvironment: A critical step in ovarian cancer metastasis. Cancers (Basel) 11, 11–21.

Barré-Sinoussi F, Montagutelli X (2015). Animal models are essential to biological research: Issues and perspectives. Future Science OA 1, 1–3.

Bast RC, Hennessy B, Mills GB (2009). The biology of ovarian cancer: New opportunities for translation. Nat Rev Cancer 9, 415–428.

Beningo KA, Dembo M, Kaverina I, Small JV, Wang Y-LL (2001). Nascent focal adhesions are responsible for the generation of strong propulsive forces in migrating fibroblasts. The Journal of Cell Biology 153, 881–887.

Cannistra SA (2004). Cancer of the Ovary. New England Journal of Medicine 351, 2519–2529.

Carey SP, Kraning-Rush CM, Williams RM, Reinhart-King CA (2012). Biophysical control of invasive tumor cell behavior by extracellular matrix microarchitecture. Biomaterials 33, 4157–4165.

Carlsen J, Ewertsen C, Sletting S, Vejborg I, Schäfer F, Cosgrove D, Bachmann Nielsen M (2015). Ultrasound elastography in breast cancer diagnosis. ultraschall in der medizing. Ultraschall Med 36, 550–565.

Cohen CA, Shea AA, Heffron CL, Schmelz EM, Roberts PC (2016). Interleukin-12 immunomodulation delays the onset of lethal peritoneal disease of ovarian cancer. J Interferon Cytokine Res 36, 62–73.

Cohen CA, Shea AA, Lynn Heffron C, Schmelz EM, Roberts PC (2013). The parity-associated microenvironmental niche in the omental fat band is refractory to ovarian cancer metastasis. Cancer Prev Res 6, 1182–1193.

Compton SLE, Pyne ES, Liu L, Guinan J, Shea AA, Grieco JP, Frisard MI, Schmelz EM (2021). Adaptation of metabolism to multicellular aggregation, hypoxia and obese stromal cell incorporation as potential measure of survival of ovarian metastases. Exp Cell Res 399, 112397.

Condeelis J, Segall JE (2003). Intravital imaging of cell movement in tumours. Nat Rev Cancer 3, 921–930.

Coopman PJ, Do MT, Thompson EW, Mueller SC (1998). Phagocytosis of cross-linked gelatin matrix by human breast carcinoma cells correlates with their invasive capacity. Clin Cancer Res 4, 507–515.

Creekmore AL, Lynn Heffron C, Brayfield BP, Roberts PC, Schmelz EM (2013). Regulation of cytoskeleton organization by sphingosine in a mouse cell model of progressive ovarian cancer. Biomolecules 3, 386–407 3, 386–407.

Creekmore AL, Silkworth WT, Cimini D, Jensen RV, Roberts PC, Schmelz EM (2011). Changes in gene expression and cellular architecture in an ovarian cancer progression model. PLoS One 6, 1–16.

Darling EM, Zauscher S, Block JA, Guilak F (2007). A thin-layer model for viscoelastic, stress-relaxation testing of cells using atomic force microscopy: Do cell properties reflect metastatic potential? Biophys J 92, 1784–1791.

Dinkelspiel HE, Champer M, Hou J, Tergas A, Burke WM, Huang Y, Neugut AI, Ananth CV, Hershman DL, Wright JD (2015). Long-term mortality among women with epithelial ovarian cancer. Gyn Oncol 138, 421–428.

Dobbie JW, Zaki M, Wilson L (1981). Ultrastructural studies on the peritoneum with special reference to chronic ambulatory peritoneal dialysis. Scott Med J 26, 213–223.

Doubeni CA, Doubeni ARB, Myers AE (2016). Diagnosis and management of ovarian cancer. Am Fam Physician 93, 937–944.

Eckert MA, Pan S, Hernandez K, Loth RM, Andrade J, Volchenboum SL, Faber P, Montag A, Lastra R, Peter ME, *et al.* (2016). Genomics of ovarian cancer progression reveals diverse metastatic trajectories including intraepithelial metastasis to the fallopian tube. Cancer Discov 6, 1342–1350.

El-Deiry WS, Goldberg RM, Lenz HJ, Shields AF, Gibney GT, Tan AR, Brown J, Eisenberg B, Heath EI, Phuphanich S, *et al.* (2019). The current state of molecular testing in the treatment of patients with solid tumors, 2019. CA Cancer J Clin 69, 350–343.

Estabridis HM, Jana A, Nain A, Odde DJ (2018). Cell migration in 1D and 2D nanofiber microenvironments. Ann Biomed Eng 46, 392–403.

Friedl P, Wolf K (2003). Tumour-cell invasion and migration: diversity and escape mechanisms. Nat Rev Cancer 3, 362–374.

Garraway LA, Lander ES (2013). Lessons from the cancer genome. Cell 153, 17–37.

Gligorijevic B, Wyckoff J, Yamaguchi H, Wang Y, Roussos ET, Condeelis J (2012). N-WASP-mediated invadopodium formation is involved in intravasation and lung metastasis of mammary tumors. J Cell Sci 125, 724–734.

Goff BA, Mandel L, Muntz HG, Melancon CH (2000). Ovarian carcinoma diagnosis. Cancer 89, 2068–2075.

Greico J, Allen ME, Perry JB, Wang Y, Song Y, Rohani A, Compton SLE, Smyth JW, Swami NS, Browm DA (2021). Progression-mediated changes in mitochondrial morphology promotes adaptation to hypoxic peritoneal conditions in serous ovarian cancer. Front Oncol 10, 1–16.

Gupton SL, Waterman-Storer CM (2006). Spatiotemporal feedback between actomyosin and focal-adhesion systems optimizes rapid cell migration. Cell 125, 1361–1374.

Hall A, Chan P, Sheets K, Apperson M, Delaughter C, Gleason TG, Phillippi JA, Nain A (2017). Nanonet force microscopy for measuring forces in single smooth muscle cells of the human aorta. Mol Biol Cell 28, 1894–1900.

Hanahan D, Weinberg RA (2011). Hallmarks of cancer: The next generation. Cell 144, 646–674.

Hauke L, Narasimhan S, Primebnig A, Kaverina I, Rehfeldt F (2021). A Focal Adhesion Filament Cross-correlation Kit for fast, automated segmentation and correlation of focal adhesions and actin stress fibers in cells. PloS One 16, 1–22.

Heath RM, Jayne DG, O'Leary R, Morrison EE, Guillou PJ (2004). Tumour-induced apoptosis in human mesothelial cells: A mechanism of peritoneal invasion by Fas Ligand/Fas interaction. Br J Cancer 90, 1437–1442.

Huang S, Arsdall M, Tedjarati S, McCarty M, Wu W, Langley R, Fidler IJ (2002). Contributions of stromal metalloproteinase-9 to angiogenesis and growth of human ovarian carcinoma in mice. J Natl Cancer Inst 94, 1134–1142.

Ince TA, Sousa A, Jones M, Harrell J, Agoston E, Krohn M, Selfors L, Liu W, Chen K, Yong M, *et al.* (2015). Characterization of twenty-five ovarian tumour cell lines that phenocopy primary tumours. Nat Commun 6, 1–14.
Indra I, Undyala V, Kandow C, Thirumurthi U, Dembo M, Beningo KA (2011). An in vitro correlation of mechanical forces and metastatic capacity. Phys Biol 8, 1–22.
Iwanicki MP, Davidowitz RA, Ng MR, Besser A, Muranen T, Merritt M, Danuser G, Ince T, Brugge JS (2011). Ovarian cancer spheroids use myosin-generated force to clear the mesothelium. Cancer Discov 1, 144–157.
Jana A, Nookaew I, Singh J, Behkam B, Franco AT, Nain AS (2019). Crosshatch nanofiber networks of tunable interfiber spacing induce plasticity in cell migration and cytoskeletal response. FASEB J 33, 10618–10632.
Jelovac D, Armstrong DK (2011). Recent progress in the diagnosis and treatment of ovarian cancer. CA Cancer J Clin 61, 183–203.
Kapoor A, Barai A, Thakur B, Das A, Patwardhan S, Monteiro M, Gaikwad S, Bukhari AB, Mogha P, Majumder A, *et al.* (2018). Soft drug-resistant ovarian cancer cells migrate via two distinct mechanisms utilizing myosin II-based contractility. Biochim Biophys Acta Mol Cell Res 1865, 392–405.
Kenny HA, Chiang C, White EA, Schryver EM, Habis M, Romero IL, Ladanyi A, Penicka CV, George J, Matlin K, *et al.* (2014). Mesothelial cells promote early Ovarian cancer metastasis through fibronectin secretion. J Clin Investig 124, 4614–4628.
Ketene AN, Roberts PC, Shea AA, Schmelz EM, Agah M (2012a). Actin filaments play a primary role for structural integrity and viscoelastic response in cells. Int J Integr Biol 4, 540–549.
Ketene AN, Schmelz EM, Roberts PC, Agah M (2012b). The effects of cancer progression on the viscoelasticity of ovarian cell cytoskeleton structures. Nanomedicine 8, 93–102.
Koons B, Sharma P, Ye Z, Mukherjee A, Lee MH, Wirtz D, Behkam B, Nain AS (2017). Cancer protrusions on a tightrope: nanofiber curvature contrast quantitates single protrusion dynamics. ACS Nano 11, 12037–12048.
Kraning-Rush CM, Califano JP, Reinhart-King CA (2012). Cellular traction stresses increase with increasing metastatic potential. PLoS One 7, 1–10.
Lawrence MS, Stojanov P, Mermel CH, Robinson JT, Garraway LA, Golub TR, Meyerson M, Gabriel SB, Lander ES, Getz G (2014). Discovery and saturation analysis of cancer genes across 21 tumour types. Nature 505, 495–501.
Lengyel E (2010). Ovarian cancer development and metastasis. Am J Pathol 177, 1053–1064.
Leong HS, Robertson AE, Stoletov K, Leith SJ, Chun CA, Chien AE, Hague MN, Ablack A, Carmine-Simmen K, McPherson VA, *et al.* (2014). Invadopodia are required for cancer cell extravasation and are a therapeutic target for metastasis. Cell Reports 8, 1558–1570.
Liu W, Cheng S, Asa SL, Ezzat S (2008). The Melanoma-associated antigen a3 mediates fibronectin-controlled cancer progression and metastasis. Cancer Res 68, 8104–8116.
Martić-Kehl MI, Schibli R, Schubiger PA (2012). Can animal data predict human outcome? Problems and pitfalls of translational animal research. Eur J Nucl Med Mol Imaging 39, 1492–1496.
Meehan S, Nain AS (2014). Role of Suspended Fiber Structural Stiffness and Curvature on Single-Cell Migration, Nucleus Shape, and Focal-Adhesion-Cluster Length. Biophysical Journal 107, 2604–2611.
Meirson T, Gil-Henn H, Samson AO (2020a). Invasion and metastasis: the elusive hallmark of cancer. Oncogene 39, 2024–2026.
Meirson T, Gil-Henn H, Samson AO (2020b). Invasion and metastasis: the elusive hallmark of cancer. Oncogene 39, 2024–2026.
Merritt MA, Bentink S, Schwede M, Iwanicki MP, Quackenbus J, Woo T, Agoston ES, Reinhardt F, Crum CP, Berkowitz RS, *et al.* (2013). Gene expression signature of normal cell-of-origin predicts ovarian tumor outcomes. PLoS One 8, e80314.
Mukherjee A, Behkam B, Nain AS (2019). Cancer cells sense fibers by coiling on them in a curvature-dependent manner. IScience 19, 905–915.
Munevar S, Wang YL, Dembo M (2001). Traction force microscopy of migrating normal and H-ras transformed 3T3 fibroblasts. Biophys J 80, 1744–1757.
Nain AS, Sitti M, Jacobson A, Kowalewski T, Amon C (2009). Dry spinning based spinneret based tunable engineered parameters (STEP) technique for controlled and aligned deposition of polymeric nanofibers. Macromol Rapid Commun 30, 1406–1412.
Nain AS, Wang J (2013). Polymeric nanofibers: isodiametric design space and methodology for depositing aligned nanofiber arrays in single and multiple layers. Polym J 451, 695–700.
Niedbala MJ, Crickard K, Bernacki RJ (1985). Interactions of human ovarian tumor cells with human mesothelial cells grown on extracellular matrix. An in vitro model system for studying tumor cell adhesion and invasion. Exp Cell Res 160, 499–513.
Ning Y, Manegold PC, Hong YK, Zhang W, Pohl A, Lurje G, Winder T, Yang D, LaBonte MJ, Wilson PM, *et al.* (2011). Interleukin-8 is associated with proliferation, migration, angiogenesis and chemosensitivity in vitro and in vivo in colon cancer cell line models. Int J Cancer 128, 2038–2049.
Novak C, Horst E, Mehta G (2018). Review: Mechanotransduction in ovarian cancer: Shearing into the unknown. APL Bioeng 2, 1–25.
Ozga M, Aghajanian C, Myers-Virtue S, McDonnell G, Jhanwar S, Hichenberg S, Sulimanoff I (2013). A systematic review of ovarian cancer and fear of recurrence. Palliat Support Care 13, 1771–1780.
Padhi A, Singh K, Franco-Barraza J, Marston DJ, Cukierman E, Hahn KM, Kapania RK, Nain AS (2020a). Force-exerting perpendicular lateral protrusions in fibroblastic cell contraction. Commun Bio 3, 1–11.
Padhi A, Thomson AH, Perry JB, Davis GN, McMillan RP, Loesgen S, Kaweesa EN, Kapania R, Nain AS, Brown DA (2020b). Bioenergetics underlying single-cell migration on aligned nanofiber scaffolds. Am J Physiol Cell Physiol 318, C476–C485.
Papageorgis P, Lambert AW, Ozturk S, Gao F, Pan H, Manne U, Alekseyev YO, Thiagalingam A, Abdolmalekym HA, Lenburg M, *et al.* (2010). Smad Signaling Is Required to Maintain Epigenetic Silencing during Breast Cancer Progression. Mol Cell Pathobiol 70, 968–978.
Pepin KM, Ehman RL, McGee KP (2015a). Magnetic resonance elastography (MRE) in cancer: Technique, analysis, and applications. Prog Nucl Magn Reson Spectrosc 90–91, 32–48.
Phillip JM, Wu P, Gilkes DM, Williams W, McGovern S, Daya J, Chen J, Aifuwa I, Lee JSH, Gan R, *et al.* (2017). Biophys biomolecular determination of cellular age in humans. Nature Biomed Eng 1, 0093.
Phillips-Chavez C, Watson M, Coward J, Schloss J (2020). A systematic literature review assessing if genetic biomarkers are predictors for platinum-based chemotherapy response in ovarian cancer patients. Eur Journ Clin Pharm 76, 1059–1074.
Plotnikov SV, Pasapera AM, Sabass B, Waterman CM (2012). Force fluctuations within focal adhesions mediate ECM-rigidity sensing to guide directed cell migration. Cell 151, 1513–1527.
Reig G, Pulgar E, Concha ML (2014). Cell migration: from tissue culture to embryos. Development 141, 1999–2013.
Roberts PC, Mottillo EP, Baxa AC, Heng HHQ, Doyon-Reale N, Gregoire L, Lancaster WD, Rabah R, Schmelz EM (2005). Sequential molecular and cellular events during neoplastic progression: A mouse syngeneic ovarian cancer model. Neoplasia 7, 944–956.
Rojas V, Hirshfield K, Ganesan S, Rodriguez-Rodriguez L (2016). Molecular characterization of epithelial ovarian cancer: implications for diagnosis and treatment. Int J Mol Sci 17, 1–23.
Rösel D, Brabek J, Tolde O, Mierke CT, Zitterbard DP, Raupach C, Bicanova K, Kollmannsberger P, Pankova D, Vesely P, *et al.* (2008). Up-regulation of Rho/ROCK Signaling in sarcoma cells drives invasion and increased generation of protrusive forces. Mol Cancer Res 6, 1410–1430.
Rustin G (2002). CA125 response: can it replace the traditional response criteria in ovarian cancer? Oncologist 7, 437–443.
Satpathy M, Shao M, Emerson R, Donner DB, Matei D (2009). Tissue transglutaminase regulates matrix metalloproteinase-2 in ovarian cancer by modulating cAMP-response element-binding protein activity. J Biol Chem 284, 15390–15399.
Sharma P, Sheets K, Elankumaran S, Nain AS (2013). The mechanistic influence of aligned nanofibers on cell shape, migration and blebbing dynamics of glioma cells. Integr Biol 5, 1036–1044.
Sheets K, Wang J, Zhao W, Kapania R, Nain AS (2016). Nanonet force microscopy for measuring cell forces. Biophys J 111, 197–207.
Sheets K, Wunsch S, Ng C, Nain AS (2013). Shape-dependent cell migration and focal adhesion organization on suspended and aligned nanofiber scaffolds. Acta Biomater 9, 7169–7177.
Steeg PS (2006). Tumor metastasis: Mechanistic insights and clinical challenges. Nature Medicine 12, 895–904.
Stoletov K, Willets L, Paproski R, Bond DJ, Raha S, Jovel J, Adam B, Robertson AE, Wong F, Woolner E, *et al.* (2018). Quantitative in vivo whole genome motility screen reveals novel therapeutic targets to block cancer metastasis. Nature Commun 9, 2343.
Thomas NW (1987). Embryology and structure of the mesothelium. In: Pathology of the Mesothelium, London: Springer, 1–13.
Tomar S, Plotnik JP, Haley J, Scantland J, Dasari S, Sheikh Z, Emerson R, Lenz D, Hollenhorst PC, Mitra AK (2018). ETS1 induction by the

microenvironment promotes ovarian cancer metastasis through focal adhesion kinase. Cancer Lett 414, 190–204.
Torre LA, Trabert B, DeSantis CE, Miller KD, Samimi G, Runowicz CD, Gaudet MM, Jemal A, Siegel RL (2018). Ovarian cancer statistics, 2018. CA Cancer J Clin 68, 284–296.
Tran AM, Chalbatani GM, Berland L, Cruz De los Santos M, Raj P, Jalali SA,Gharagouzloo, E, Ivan C, Dragomir MP, Calin GA (2020). A new world of biomarkers and therapeutics for female reproductive system and breast cancers: circular RNAs. Front Cell Dev Biol 8, 1–17.
Tu-Sekine B, Padhi A, Jin S, Kalyan S, Singh K, Apperson M, Kapania R, Hur SC, Nain A, Kim SF (2019). Inositol polyphosphate multikinase is a metformin target that regulates cell migration. FASEB J 33, 14137–14146.
Valastyan S, Weinberg RA (2011). Tumor metastasis: Molecular insights and evolving paradigms. Cell 147, 275–292.
Wang J, Nain AS (2014). Suspended micro/nanofiber hierarchical biological scaffolds fabricated using non-electrospinning STEP technique. Langmuir 30, 13641–13649.
Webb K, Hlady V, Tresco PA (2000). Relationships among cell attachment, spreading, cytoskeletal organization, and migration rate for anchorage-dependent cells on model surfaces. J Biomed Mater Res 49, 362–368.
Weinstein JN, Collisson EA, Mills GB, Mills Shaw KR, Ozenberger BA, Ellrott K,Shmulevich, I, Sander C, Stuart JM (2013). The Cancer Genome Atlas Pan-Cancer analysis project. Nat Genet 45, 1113–1120.
Wilkosz S, Ireland G, Khwaja N, Walker M, Butt R, De Giorgio-Miller A, Herrick SE (2005). A comparative study of the structure of human and murine greater omentum. Anat Embryol 209, 251–261.
Wu PH, Gilkes DM, Phillip JM, Narkar A, Cheng TWT, Marchand J, Lee MH, Li R, Wirtz D (2020). Single-cell morphology encodes metastatic potential. Sci Adv 6, eaaw6938.
Yadav S, Barton MJ, Nguyen NT (2019). Biophysical properties of cells for cancer diagnosis. J Biomechan 86, 1–7.
Yamamoto H, Sutoh M, Hatakeyama S, Hashimoto Y, Yoneyama T, Koie T, Saitoh H, Yamaya K, Funyu T, Nahamura T, *et al*. (2011). Requirement for FBP17 in Invadopodia Formation by Invasive Bladder Tumor Cells. J Urol 185, 1930–1938.
Yankaskas CL, Thompson KN, Paul CD, Vitolo MI, Mistriotis P, Mahendra A, Bajpai VK, Shea DJ, Manto KM, Chai AC, *et al*. (2019). A Microfluidic assay for the quantification of the metastatic propensity of breast cancer specimens. Nat Biomed Eng 3, 452–465.
Zijlstra A, Lewis J, DeGryse B, Stuhlmann H, Quigley JP (2008a). The inhibition of tumor cell intravasation and subsequent metastasis via regulation of in vivo tumor cell motility by the tetraspanin CD151. Cancer Cell 13, 221–234.